Polymer 50 (2009) 3386–3395

Contents lists available at ScienceDirect

Polymer

journal homepage: www.elsevier.com/locate/polymer

Micromechanics of uniaxial tensile deformation and failure in high impact polystyrene (HIPS)

Rajdeep Sharma [a,b,*], Simona Socrate [a]

[a] Department of Mechanical Engineering, Massachusetts Institute of Technology, 77 Massachusetts Avenue, Cambridge, MA 02139, USA
[b] General Electric Global Research, 1 Research Circle, Room K1-4B18, Niskayuna, NY 12309, USA

ARTICLE INFO

Article history:
Received 30 January 2009
Received in revised form
21 April 2009
Accepted 24 April 2009
Available online 12 May 2009

Keywords:
Micromechanics
Toughening
HIPS

ABSTRACT

While it is recognized that the heterogeneous particles in HIPS play the dual role of providing multiple sites for craze initiation in the polystyrene (PS) matrix and allow the stabilization of the crazing process through cavitation/fibrillation in the PB phase within the particle, the precise role of particle morphology is not well understood or quantified. This work probes the micromechanics of uniaxial tensile deformation and failure in rubber-toughened PS through axi-symmetric finite element representative volume element (RVE) models that can guide the development of blends of optimal toughness. The RVE models reveal the effect on craze morphology and toughness by various factors such as particle compliance, particle morphology, particle fibrillation and particle volume fraction. The principal result of our study is that fibrillation/cavitation of PB domains within the heterogeneous particle provides the basic key ingredient to account for the micro- and macro-mechanics of HIPS.

© 2009 Elsevier Ltd. All rights reserved.

1. Introduction

The incorporation of a rubbery phase into a brittle (craze-able) polymer matrix has long been recognized as a means to significantly toughen the material. High impact polystyrene (HIPS) is one of the most successful material systems making use of this approach. HIPS was one of the first commercial polymers that were toughened by compliant, micron-sized second-phase particles. The particles in HIPS are heterogeneous, with a characteristic "salami" morphology. The "salami" morphology consists typically of 80% volume fraction of sub-micron sized polystyrene (PS) subinclusions within 20% polybutadiene (PB), which is the topologically continuous phase (Fig. 1) [1,2]. PB in the salami particles occurs in the form of thin layers, typically of thickness 5–10 nm. The actual mechanism that governs the toughening of HIPS was first identified by Bucknall and Smith [3]. By stretching thin films (with thicknesses in the range 5–10 μm) of the blend, they found that macroscopic yielding was accompanied by the formation of multiple crazes in PS around the salami particles. Crazes are comprised of elongated voids and fibrils of highly oriented, load bearing polymeric material that are aligned in the direction of the local maximum principal stress. It is well known that crazes are both a manifestation of dilatational plasticity as well as precursors to fracture, and hence control the toughness of several nominally brittle glassy polymers such as PS, polymethylmethacrylate (PMMA) and styrene-acrylonitrile (SAN). Fig. 1(a) shows a typical stress–strain curve for HIPS, along with a micrograph showing the heterogeneous nature of the particle and multiple crazing in the PS matrix.

The previously well-accepted notion that toughening in HIPS is due to multiple crazing in the PS matrix, and that the role of the particle is simply to act as a stress concentrator and provide a multitude of preferential sites for crazing in the matrix, has been a subject of serious critical thought over the last two decades. An important early study [4], due to Bubeck et al., was based on real-time SAXS experiments on *commercially thick* HIPS tensile impact samples. Importantly, the use of SAXS technique overcame the inherent limitation of electron microscopy studies where thin specimens are needed. From the scattering measurements and analysis, Bubeck et al. were able to estimate the total inelastic strain, as well as the crazing strain. By subtracting the crazing strain from the total inelastic strain, they determined the magnitude of the inelastic strain due to non-crazing mechanisms, which in HIPS is attributed mostly to particle cavitation and elastic/inelastic bending of ligaments between cavitating particles. Bubeck et al. found that the inelastic strain due to non-crazing mechanisms exceeds the strain due to crazing (in many cases by about a factor of 2), and that the non-crazing inelastic strain precedes crazing. On lines somewhat similar to Bubeck et al., Magalhaes and Borggreve

* Corresponding author. General Electric Global Research, 1 Research Circle, Room K1-4B18, Niskayuna, NY 12309, USA. Tel.: +1 518 387 7069; fax: +1 518 387 7006.
E-mail address: sharmar@ge.com (R. Sharma).

0032-3861/$ – see front matter © 2009 Elsevier Ltd. All rights reserved.
doi:10.1016/j.polymer.2009.04.073

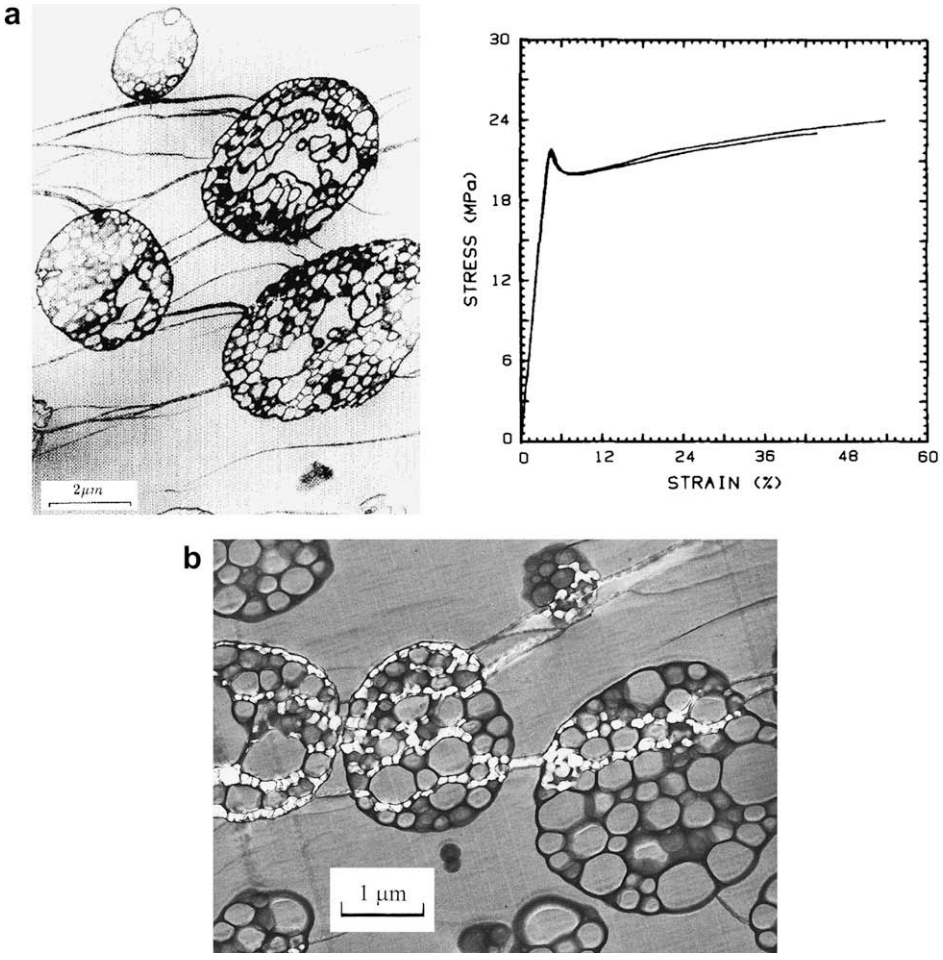

Fig. 1. (a) The stress–strain response of HIPS (right) with particle volume fraction $f_p = 0.2$, average particle size = 2.5 μm at a strain-rate = 1×10^{-4} s^{-1}. Micrograph (left) reveals the composite nature of the particle and crazing in the PS matrix (taken from Polymer, Vol. 36, 1995, pp. 2173–2180. 1995 Elsevier. Reprinted with permission of Elsevier) [1]. (b) TEM micrograph of a thin HIPS section, prepared from a tensile specimen beyond yield (taken from Journal of Microscopy, Vol. 201, 2001, pp 221–229. 2001 Wiley-Blackwell. Reprinted with permission of Wiley-Blackwell) [2].

[5] used real-time SAXS on HIPS tensile specimens subjected to quasi-static strain rates, and found that crazing accounts only for 25% of the total volume change in the specimens. TEM micrographs showing patterns of deformation in thin HIPS films are shown in Fig. 1(b) [2]; also see TEM micrographs from Cieslinski [6]. These micrographs show that particle deformation is mainly accomplished through fibrillation of the thin PB layers between PS subinclusions.

Recently, HIPS specimens were subjected to progressively higher doses of γ-radiation [7], which has the effect of increasing the crosslink density in PB (thereby minimizing or eliminating fibrillation), but has a negligible effect on PS. Increasing levels of γ-radiation were shown to result in increased yield and flow stress, and reduced toughness, and thus highlighted the important role of fibrillation on the toughening in HIPS.

To this date, very limited modeling studies have been done on HIPS that can shed light on the toughening mechanisms, and in particular on the role of particle morphology. Socrate et al. [8] developed a micromechanical model for crazing using a cohesive zone formulation, and applied their model to a preliminary study of HIPS, in which the composite "salami" particle was represented by its homogenized, elastic properties, and hence did not address the role of particle morphology and particle cavitation on the deformation and toughness of HIPS. Recently, Zairi et al. [9,10] have modeled the overall constitutive stress–strain behavior of the rubber-toughened polymers – PMMA and PS – using a viscoplastic damage model within the Gurson–Tvergaard micromechanical framework. While model predictions were in quantitative agreement with experimental macroscopic response, the proposed approach does not address the role of particle morphology on the deformation and toughening of HIPS. The objective of our study is to clarify and quantify the precise role of particle morphology on the micromechanics and macromechanics of uniaxial tensile deformation and failure in rubber-toughened PS. In particular, this study seeks to investigate the role of particle compliance, particle heterogeneity and particle cavitation/fibrillation.

2. Model

In order to investigate the local mechanisms that govern the deformation and failure of HIPS, a micromechanical model that adequately captures the particle morphology is proposed. The definition of a micromechanical model requires two components: (i) the geometric description of the representative volume element (RVE) and, (ii) the constituent behavior of its three phases – the PS matrix, the PS subinclusions within the particle, and the PB layers within the particle.

Although limited findings of particle/matrix debonding in experimental blends have been reported in the literature [11,12], we note that due to the chemical grafting of the PB and PS phases

during the manufacturing of HIPS, the interface between the HIPS particle and the PS matrix is very strong and particle/matrix debonding is not typically observed in commercial blends. Accordingly, we neglect the possibility of particle/matrix decohesion and idealize the interface as perfectly bonded. Generally speaking, matrix–particle adhesion is critical for toughening in HIPS, as it provides not only adequate stress transfer between the particle and the matrix needed for initiation of multiple crazes in the matrix, but also ensures the stable thickening of crazes between any two particles.

2.1. Geometry of the RVE

Similar to other particle composites, micrographs of HIPS reveal statistical distributions in several morphological features such as particle size and shape, and spatial variations in inter-particle spacing with possibility of particle clustering even in well-dispersed systems. HIPS systems present additional complexity in that the particles are themselves 2-phase composites: the volume fraction and spatial arrangement of the PB and PS phase exhibit some statistical variations between particles. The task of modeling these complex features can be greatly simplified by selecting a RVE for the material. In its simplest embodiment, this RVE contains a single particle surrounded by PS matrix. The basic key interactions with neighboring particles are simulated by imposing appropriate periodic boundary conditions on the RVE model.

The one-particle RVE model used in our HIPS studies was proposed by Socrate and Boyce [13], and is an axisymmetric equivalent to the Voronoi tessellation of a Body Centered Cubic (V-BCC) array of voids/particles. In simulations of porous PC, Socrate and Boyce found that the numerical predictions of the axisymmetric V-BCC model provide reasonable agreement with experimental results and are superior to those provided by the traditional axisymmetric Stacked Hexagonal Array (SHA) model, especially at high void volume fractions and high triaxiality. Fig. 2 shows the deformed configuration of the axisymmetric V-BCC cell, along with one of its periodic neighbors, which is identical to the parent cell but rotated by 180° in the r–z plane. A characteristic feature of this model is the staggered arrangement of particles in the r–z plane, which is closer to the morphology of particle composites, compared to the SHA model, in which the particles are aligned in the equatorial plane. A notable drawback of the axisymmetric V-BCC model is that it cannot correctly account for transverse shear effects. However, despite this, it provides a judicious computational route to modeling particle composites under axisymmetric loading conditions. We note that in a recent study [14] the staggered axisymmetric RVE employed in our study was shown to provide results in good agreement with those obtained with a fully three-dimensional model, while affording increased computational efficiency. The boundary conditions needed to simulate the staggered arrangement of particles were given by Tvergaard [15,16] in his study of cavity growth and interaction between small and large voids, and also subsequently by others [13,17,18].

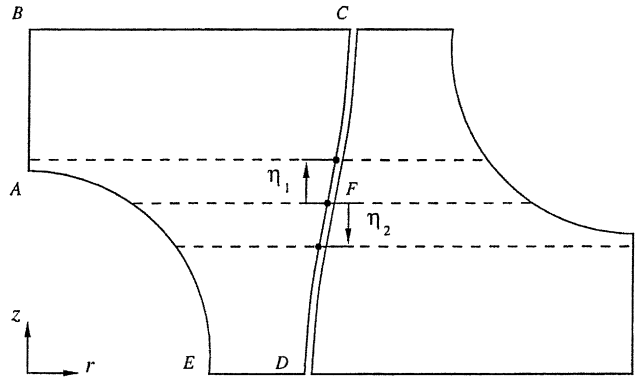

Fig. 2. Axisymmetric V-BCC cell in the deformed configuration, along with a periodic neighbor.

Operationally, in our simulations the top plane of the RVE is driven by an axial displacement history, $u_Z(t)|_B$, that produces a constant applied axial strain rate, $\dot{E}_Z$, on the RVE. The axial reaction force corresponding to node B, $P_z|_B$, is used to determine the axial component of the macroscopic Cauchy stress, Σ_z, by

$$\Sigma_z \equiv \frac{1}{V}\int_{x\in V} \sigma_{zz}(x)dV = \frac{P_z|_B}{\pi[R_0+u_r|_F]^2} \tag{1}$$

where $\pi[R_0+u_r|_F]^2$ is the average, deformed cross sectional area of the RVE. The macroscopic axial strain, E_z, is calculated from the height of the RVE in the deformed configuration, H, and the initial RVE height, H_0:

$$E_z = \ln\left(\frac{H}{H_0}\right) = \ln(1+u_z|_B) \tag{2}$$

The macroscopic volumetric strain, E_v, is given by the logarithmic ratio of the deformed RVE volume, V, to the initial volume, $V_0 = \pi R_0^2 H_0$:

$$E_v = \ln\left(\frac{V}{V_0}\right) = \ln\left(\frac{(R_0+u_r|_F)^2(1+u_z|_B)}{R_0^2 H_0}\right) \tag{3}$$

In the RVE studies, the inelastic volumetric strain of the particle, $E_{v(particle)}$, and the matrix, $E_{v(matrix)}$, are defined as:

$$E_{v(particle)} = \ln\left(1+\frac{\phi_{fib}}{V_0}\right) \tag{4}$$

$$E_{v(matrix)} = \ln\left(1+\frac{\phi_{craze}}{V_0}\right) \tag{5}$$

where ϕ_{fib} and ϕ_{craze} represent respectively the volume of the fibrillated PB domains and the crazed PS matrix.

The RVE topology of composites investigated in our studies can be classified into two types – RVEs with homogeneous particles, and RVEs with heterogeneous particles consisting of 70% PS sub-inclusions within 30% topologically continuous PB. The particle size is kept fixed at 1.5 μm for all RVEs. Models are developed for three different particle volume fractions: $f_p = 0.08$, 0.18, 0.28 by appropriately increasing the size of the RVE. In all cases, the initial aspect ratio of the RVE is given by $R_0/H_0 = 1$, and the macroscopic applied tensile strain rate is $\dot{E}_z = 1\times10^{-3}\ \mathrm{s}^{-1}$.

The geometry of the axisymmetric RVEs, for $f_p = 0.28$, is shown in Fig. 3. The RVE with the homogeneous particle (Fig. 3a) is used to study the effect of particle compliance on the toughening of PS. The RVE with the particle explicitly decomposed in PS and PB domains (Fig. 3b) is used in two parallel studies: a study on the effects of particle heterogeneity (where "no fibrillation" was allowed in the PB domains), and a study on the effect of PB fibrillation. We note that while the actual thickness of the PB phase in the particle is in the range 5–10 nm, the PB element size is about 25 nm; meshing considerations necessitated this approximation. RVE studies in this work were performed using the finite element software ABAQUS™.

As can be seen from Fig. 3, our model studies use spherical particles. We note that the particle shape affects the stress state both in the PS matrix and within the particle itself. Since initiation of particle cavitation and matrix crazing is stress-dependent, model

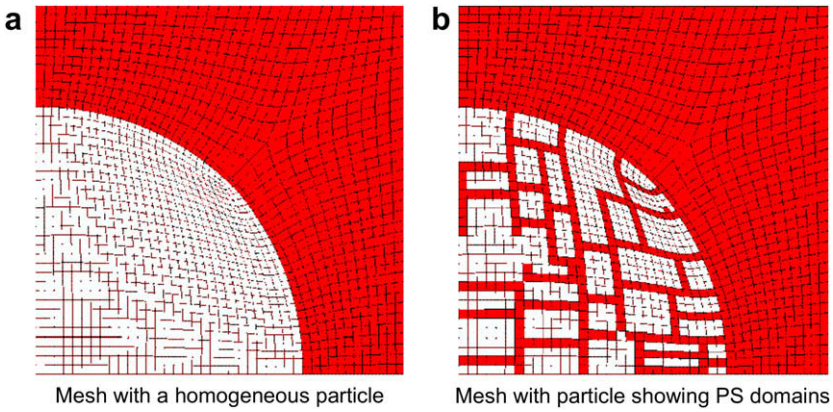

Fig. 3. Axisymmetric RVE geometry for the homogeneous particle and the heterogeneous particle. PS subinclusions in (b) are shown in white.

predictions are expected to be dependent on particle shape [19]. However, we note that the particles in HIPS blends are approximately spherical, and small deviations from the equiaxial configuration have minor effects on the stress fields.

2.2. Constitutive model for the particle

For a parametric study on the effect of particle compliance on toughness, the particle was modeled as linear elastic with shear modulus, G_p, and bulk modulus, K_p. Table 1 indicates that in the parametric study, K_p was kept equal to $K_{PB} = 1940$ MPa (the bulk modulus of PB), while G_p was progressively increased in factors of 10 from $G_{PB} = 0.62$ MPa (the shear modulus of PB) to 620 MPa; the elastic properties of PB were taken from Boyce et al. [20]. The particle Young's modulus, E_p and the Poisson's ratio, ν_p, are also given in Table 1 for convenience. In addition to the parametric study on particle compliance, we show results of a study in which the salami particle was represented by its homogenized elastic properties: $K_p^H = 1940$ MPa and $G_p^H = 111$ MPa, where the latter estimate is obtained from Argon et al. [21].

For studies with an inhomogeneous particle topology, the constitutive description of the particle is given in terms of the response of the (non-crazeable) PS subinclusions, and the response of the topologically continuous PB domain. The non-crazeable PS within the particle is modeled as linear elastic with bulk modulus, K_{PS}, and shear modulus, G_{PS}, given in Table 2 (e.g., [8]). PB is considered to be a compressible, rubber-elastic material with a constitutive representation that follows the framework originally introduced by Arruda and Boyce [22]. The Cauchy stress, $\mathbf{T}^{\mathbf{N}}$, reflects the effects of network orientation:

$$\mathbf{T}^{\mathbf{N}} = J^{-1}\mu_r \frac{\sqrt{N}}{\bar{\lambda}_{chain}} L^{-1}\left(\frac{\bar{\lambda}_{chain}}{\sqrt{N}}\right)\mathrm{dev}(\bar{\mathbf{B}}) + K_{PB}(J-1). \tag{6}$$

Here, μ_r is the initial hardening modulus taken to be equal to $G_{PB}/3$, N is the number of rigid molecular units between entanglements, $J = \det\ \mathbf{F}$ (where $\mathbf{F}$ is the deformation gradient), $\bar{\mathbf{F}} = J^{-1/3}\mathbf{F}$, $\bar{\mathbf{B}} = \bar{\mathbf{F}}\bar{\mathbf{F}}^{\mathbf{T}}$, and $\bar{\lambda}_{chain} = (\mathrm{tr}[\bar{\mathbf{B}}]/3)^{1/2}$. L^{-1} is the inverse Langevin function, where $L(\beta) = \coth(\beta) - 1/\beta$ and $\beta = L^{-1}(\bar{\lambda}_{chain}/\sqrt{N})$. The inverse Langevin function becomes unbounded as the effective chain stretch $\bar{\lambda}_{chain}$ approaches the locking stretch, $\sqrt{N}$, and hence accounts for finite chain extensibility as well as the strong orientation hardening observed in elastomers at large strains. Fibrillation of the PB phase is a result of the formation of nano-scale voids, which effectively eliminate the resistance of PB to volumetric expansion. Before fibrillation, $K_{PB}/\mu_r = 9375$ is governed by the isotropic elastic properties of bulk PB. After fibrillation, we take $K_{PB}/\mu_r = 1$, i.e., we reduce the bulk stiffness of the fibrillated PB by about 4 orders of magnitude; the non-zero value of K_{PB} after fibrillation provides numerical stability to the fibrillated finite element. Fibrillation is taken to occur when the local hydrostatic stresses reaches a critical value, σ_{fib}

$$\sigma_h \geq \sigma_{fib} \tag{7}$$

Gent and coworkers [23,24] have estimated that failure in bulk rubber specimens occurs at a critical hydrostatic stress of $\sim 5E/6$ (where E is the small strain Young's modulus of rubber). Since $E_{PB} = 1.86$ MPa [20], the bulk fibrillation stress in PB is estimated to be $\sigma_{fib} = 1.5$ MPa. A representative value for elastomers of $N = 25$ is used for PB. The properties of PB used in this work are indicated in Table 2.

2.3. Constitutive model for the PS matrix

Since the PS matrix deforms inelastically by crazing, the constitutive characterization of the PS matrix requires modeling of the three stages of crazing – initiation, growth, and breakdown. The physics of crazing has been extensively discussed in innumerous publications, and summarized in several excellent reviews [25–30]. Detailed, numerical studies that incorporate the physics of crazing within a cohesive zone framework have been performed by Van der Giessen and coworkers [31–33] to study Mode I crack-tip plasticity, and by Socrate et al. [8] to investigate matrix crazing in HIPS where the heterogeneous salami particle was modeled by its effective elastic properties. Gearing and Anand [34] developed a macroscopic continuum model for both crazing and shear yielding, and

Table 1
Particle elastic properties used to investigate the role of particle compliance on the deformation and toughness of rubber-toughened PS.

K_p (MPa)	G_p (MPa)	E_p (MPa)	ν_p
1940	0.62	1.86	0.4998
1940	6.2	18.58	0.4984
1940	62	184.04	0.4842
1940	620	1680.93	0.3556
$K_p^H = 1940$	$G_p^H = 111$	326.77	0.4719

Table 2
Material properties of the constituents of the inhomogeneous particle.

PS subinclusions		PB domains				
K_{PS} (MPa)	G_{PS} (MPa)	K_{PB} (MPa)	G_{PB} (MPa)	μ_r (MPa)	N	σ_{fib} (MPa)
2500	1150	1940	0.62	0.21	25	1.5

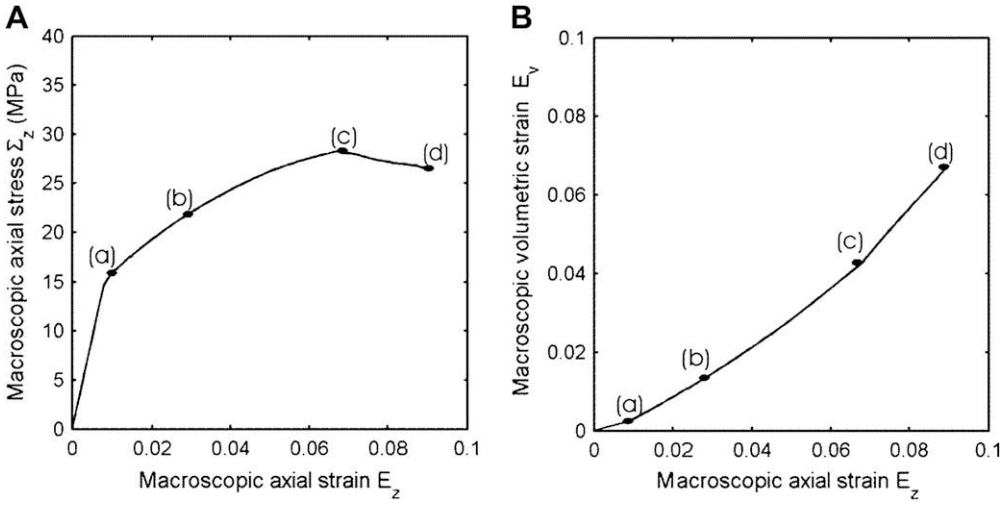

Fig. 4. Macroscopic response for RVE with PB particle $G_p = 0.62$ MPa ($f_p = 0.28$).

applied it to numerical studies on notched specimens. In a recent study on the effect of inelastic interactions of crazing and shear yielding on the toughness of laminated polymeric composites, Sharma et al. [35] extended the micromechanical cohesive zone craze model of Socrate et al. to a continuum craze model that retains the critical micromechanical features of the original model, while introducing spatial flexibility to the crazing process.[1] The crazing model for the PS matrix is based on the work of Sharma et al., and the material properties are taken from [27,36].

3. Results

The objective of the finite element RVE studies is to understand the role of particle morphology on the deformation and toughness of HIPS. This goal is accomplished by investigating the effects of:

- *particle compliance* through a parametric study on homogeneous particles, whose compliances are systematically varied.
- *particle heterogeneity* by comparing the response of the RVE with homogenized particle vs. heterogeneous particle (with no fibrillation)
- *particle fibrillation* by comparing the response of the RVE with a non-fibrillating heterogeneous particle vs. a fibrillating particle.

3.1. Study on compliant, homogeneous particles

In order to study the effect of particle compliance on the deformation and toughness of the composite, a parametric study was conducted on RVEs with $f_p = 0.28$, wherein the particle shear modulus was systematically varied, as shown in Table 1.

3.1.1. Detailed analysis for PB particle

Here, we perform a detailed investigation of the macroscopic response of the RVE with a PB particle ($G_p = 0.62$ MPa) and the underlying features of the deformation. Fig. 4 shows the macroscopic response of the RVE with a PB particle. Fig. 5 shows contour plots of craze nucleation "damage" $D(t) \equiv \int_0^t dt'/t_i(t')$, where t_i is craze initiation time associated with a fixed stress state [35]. A contour level of $D = 1$ indicates a nucleated craze; $D < 1$ indicates no crazing. Contour plots are presented for each of the macroscopic strain levels marked (a)–(d) on the Σ_z–E_z plot of Fig. 4(A).

Due to the stress concentration in PS matrix introduced by the compliant PB particle, crazing initiates at the particle–matrix interface at the equator (as shown in Fig. 5(a)), and results in deviation from linearity of the Σ_z–E_z response. The softening of the craze element after nucleation [35] provides a stress concentration for the lateral propagation of the craze. The macroscopic stress Σ_z continues to rise at points (b) and (c), despite the progression of crazing in the PS matrix, due to increasing levels of axial stress in the particle. At point (c), Σ_z reaches its peak value. Both the local axial stress and the local hydrostatic stress in the particle reach their peak value of $\cong$36 MPa, with a slightly higher stress of $\cong$38 MPa at the equator, adjacent to the interface. At point (c), the craze has fully bridged the ligament between nearby particles. Between points (c) and (d), Σ_z drops due to crazing along the particle, relieving the high axial stress in the particle. Contour plots at points (c) and (d) show large distortions in particle elements close to the interface, at the equator due to the extensive opening of the adjoining craze element.

In view of the large stresses in the particle at point (c) mentioned above, the particle is likely to undergo degradation/cavitation, particularly at the region adjoining the equatorial craze. Hence, the Σ_z–E_z response beyond (c) is unrealistic. The localized

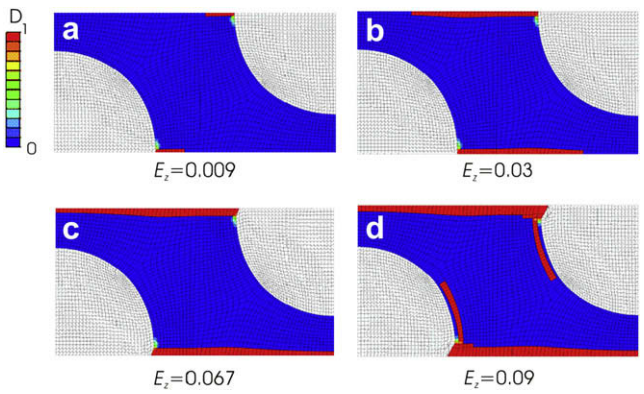

Fig. 5. Contour plots of the craze profile for $G_p = 0.62$ MPa (corresponding to Fig. 4).

[1] While the model of Socrate et al. [8] considered only craze initiation and growth, Sharma et al. [35] also incorporated craze breakdown into their craze model.

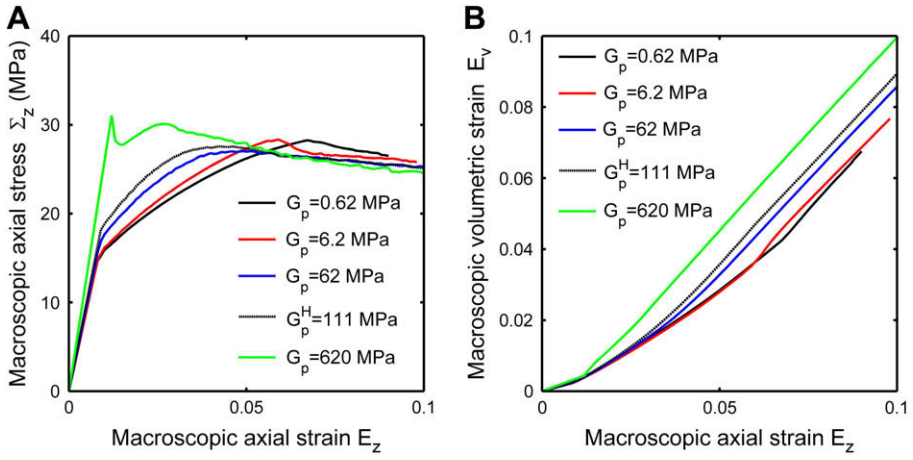

Fig. 6. The macroscopic RVE response for particle volume fraction of $f_p = 0.28$, as a function of particle shear modulus G_p.

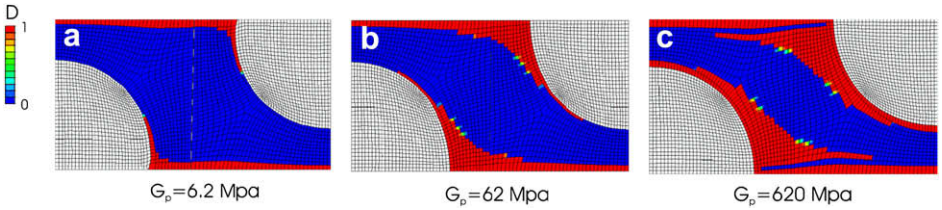

Fig. 7. Comparison of the contour plots, corresponding to Fig. 6, of the craze profile for $G_p = 6.2$, 62, 620 MPa at an axial strain $E_z = 0.067$.

nature of crazing in conjunction with the high stresses in the particle would lead to loss of structural integrity of the RVE at $E_z \leq 0.067$.

3.1.2. Discussion of parametric study on compliant, homogeneous particles

Fig. 6(A) and (B) respectively shows the evolution of the macroscopic true axial stress Σ_z and the macroscopic true volumetric strain E_v, with the macroscopic true axial strain E_z. The Σ_z–E_z responses for composites corresponding to compliant particles with $G_p = 0.62$, 6.2, 62 MPa exhibit an initial linear elastic behavior, followed by departure from linearity and a non-linear rise to a peak stress, and finally followed by softening. The notable absence of a non-linear rise to peak stress for the case $G_p = 620$ MPa is a result of delayed craze initiation in the matrix,[2] which allows a linear rise in particle axial stress with E_z. Craze initiation at $E_z = 0.012$ is followed by rapid craze propagation that relieves the high axial stress in the particle for the $G_p = 620$ MPa case, resulting in a softening macroscopic behavior immediately after craze initiation (see Fig. 6(A)). The E_v–E_z curves show a monotonic increase in E_v for all composites. Small differences in the magnitude of E_v (at a fixed E_z) indicate that the amount of axial deformation that is accommodated by particle shearing increases slightly with increasing particle compliance.

Fig. 7 shows the craze morphology for RVEs with particle stiffness $G_p = 6.2$, 62, 620 MPa, and can be compared with the craze morphology for the RVE with PB particle shown in Fig. 5. A characteristic feature of the craze morphology for these RVEs is the process of crazing around the circumference of the particle, in order to relieve the axial stress build-up in the particle. The crazing, particularly in Fig. 7(b) and (c), shows very diffused and unrealistic crazing, because the equatorial stress concentration is diminished as the compliance of the particle approaches the compliance of the matrix. The results of this study provide a micromechanical explanation of the low toughening potency of homogeneous PB particles. TEM micrographs of homogeneous PB particles [37] show that the elongation of the particle in the direction of the tensile load is accompanied by an equatorial contraction resulting in the debonding of the particle from the matrix. The large voids formed as a result of debonding result in early failure of the composite. In our study, particle–matrix compatibility prevents debonding, with the consequence that unrealistic crazing occurs in the PS matrix to accommodate the deformation.

3.2. Response of RVE with heterogeneous particle (no fibrillation)

To investigate the role of particle heterogeneity on the micro- and macro-mechanics of HIPS, the particle is modeled as a 2-phase composite comprising PS subinclusions and PB. Fibrillation in the PB domains is suppressed. Fig. 8 shows the Σ_z–E_z and E_v–E_z response, and Fig. 9 shows corresponding contour plots for the craze profile. Crazing initiates in the matrix at point (a) ($E_z = 0.01$) adjacent to the PB region, a feature that is seen often in thin-film micrographs. The initial low stiffness of the PB regions induces a local stress concentration in the matrix and provides preferential sites for crazing in the PS matrix. At point (b) ($E_z = 0.045$), which is associated with the macroscopic yield, a craze has spanned the net section of the RVE. More realistic craze patterns are predicted, compared to the studies in previous sections, in that crazes tend to

[2] Based on Goodier's solution, Boyce et al. [20] have given $\sigma_e/\sigma_\infty = 1.730$ and $\sigma_h/\sigma_\infty = 0.735$ for PB particle within a PS matrix in an infinite body subjected to a far field uniaxial stress σ_∞. Here σ_e and σ_h represent the von-Mises stress and the hydrostatic stress in the matrix just outside the particle at the equator. For a less compliant particle with $K_p = 2880$ MPa and $G_p = 880$ MPa, we have $\sigma_e/\sigma_\infty = 1.130$ and $\sigma_h/\sigma_\infty = 0.407$. While these values are not exactly true for our case of a periodic RVE with a given volume fraction of particles, they qualitatively show that with decreasing particle compliance (relative to the PS matrix), the stress concentration, in the matrix just outside the particle at the equator, decreases; this delays the initiation of crazes for the less compliant particles.

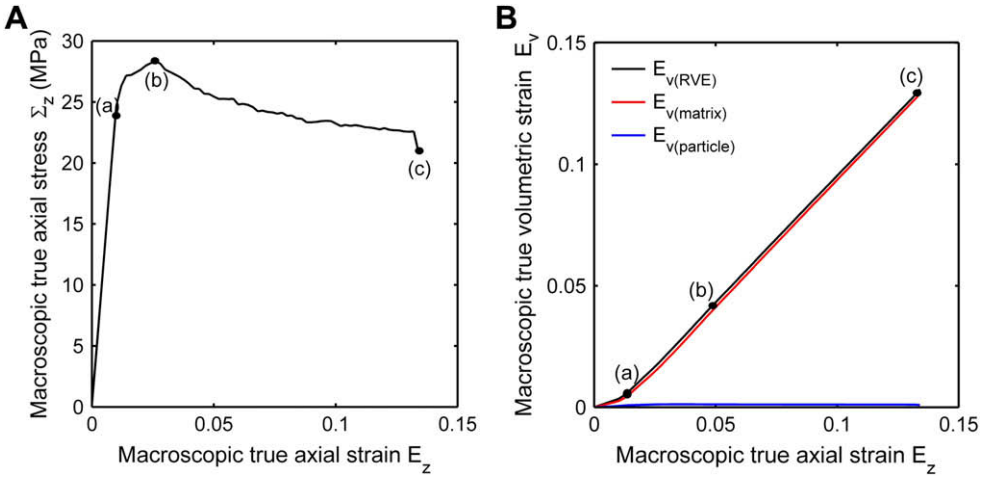

Fig. 8. The macroscopic RVE response and contour plots of the craze profile for particle volume fraction of $f_p = 0.28$. The particle is modeled as a 2-phase system, but with no fibrillation in the PB domains.

initiate adjacent to PB regions in the particle. The significant difference in volumetric compliance between the (crazeable) PS matrix and the (non-fibrillating) particle generates an inherent incompatibility between the radial stretches of matrix and particle. The PS matrix accommodates the applied axial stretch by inelastic (crazing) deformation at negligible radial stretch. On the other hand, the particle cannot accommodate a comparable axial stretch without a significant reduction in radius. The enforced radial compatibility between the particle and matrix domains limits the axial deformation of the particle.

It is energetically more favorable for the axial stretch to be almost entirely accommodated by the PS matrix through pervasive crazing, as well as crazing along the particle circumference. It is not surprising, therefore, that $E_{v(particle)} \cong 0$ (see Fig. 8(B)) for the non-fibrillating particle (as well as for homogeneous/homogenized particles studied in previous sections). At point (c) ($E_z = 0.134$), PS matrix elements have met the craze breakdown condition adjacent to the pole of the particle, resulting in crack initiation in the matrix. Pervasive and unrealistic crazing is seen in the matrix. It is noted that the post-yield softening behavior is an indication of instability in the Σ_z–E_z response, and that in reality should lead to localization of deformation and rapid failure after the peak stress is reached. Results of this study indicate that particle heterogeneity is a key feature to generating multiple crazes from a particle, but it alone cannot explain the macroscopic response of HIPS and, in particular, the experimentally observed craze profile.

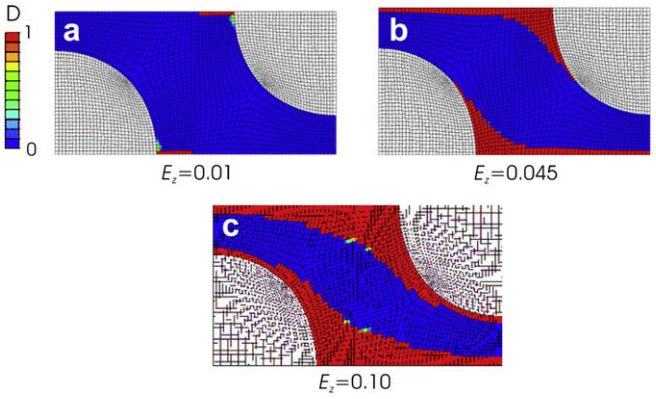

Fig. 9. Contour plots of the craze profile (corresponding to Fig. 8) for particle volume fraction of $f_p = 0.28$. The particle is modeled as a 2-phase system, but with no fibrillation in the PB domains.

3.3. Response of RVE with heterogeneous particle (with fibrillation)

In this study, the additional feature of fibrillation of PB domains is incorporated in the investigation of the effects of heterogeneous particles. The predicted Σ_z–E_z and E_v–E_z responses are shown in Fig. 10 and capture the typical macroscopic response of HIPS. The predicted E_v–E_z response (Fig. 10(B)), displays a slope of nearly unity reflecting the very limited RVE lateral contraction during tensile loading. This prediction is consistent with creep experiments on HIPS [38], as well as with data by G'Sell et al. [39]. In line with the SAXS results [4,5], a substantial amount of the total volumetric strain is accommodated by non-crazing mechanisms, i.e., by particle cavitation. However, in contrast to the these experimental findings, model predictions indicate that volume change due to crazing is predominant. This discrepancy can be probably ascribed to the meshing of the PB domains, where an element thicknesses of about 25 nm was used, while the actual thickness of PB domains is in the 5–10 nm range. It is worth noting that E_v–E_z behavior is well predicted for all particle morphologies considered in our studies: the dilatant nature of crazing always results in negligible lateral contraction of the RVE; however, models accounting for particle fibrillation can satisfy compatibility constraints between particle and matrix without introducing debonding through interfacial crazing.

At point (a) ($E_z = 0.002$), fibrillation in the particle can be seen in the contour plots of Fig. 11. Crazing in the matrix initiates at point (b) ($E_z = 0.008$). It is noted that in our previous studies, crazing initiated at $E_z = 0.01$. This highlights the potential role of fibrillation in the PB domains as a source for craze nucleation in the PS matrix: PB fibrillation allows crazing to occur earlier by providing local stress concentrations in the matrix. At point (c) ($E_z = 0.022$) associated with peak Σ_z, crazes begin to extend from one particle to another. At point (d) ($E_z = 0.1$), crazes bridge the inter-particle ligaments and thicken in the local, maximum principal stress direction. Craze breakdown at point (e) ($E_z = 0.294$) results in crack initiation in the matrix. Between points (e) and (f) ($E_z = 0.35$), Σ_z decreases as the matrix cracks progressively due to craze breakdown.

Comparison of the macroscopic response and the contour plots for heterogeneous particle RVEs with and without fibrillation,

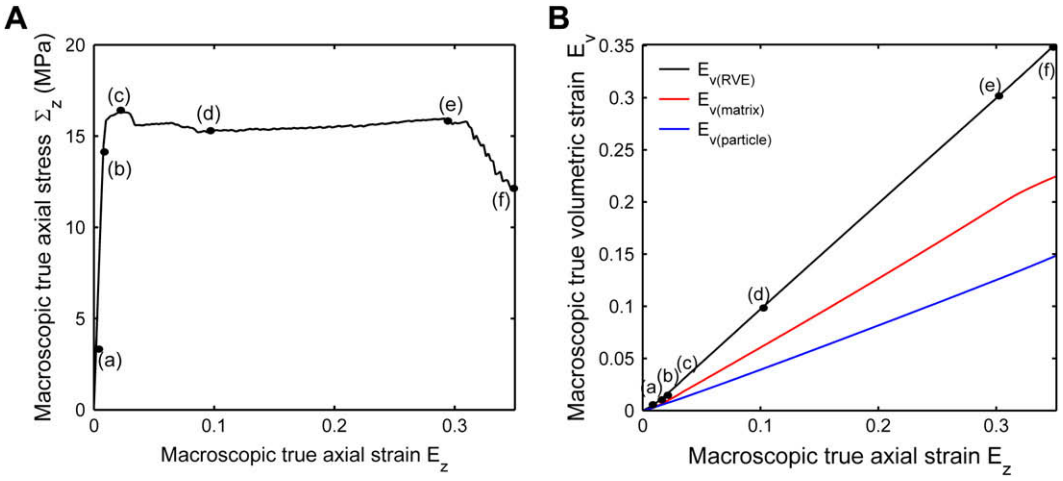

Fig. 10. Macroscopic RVE response (left) for particle volume fraction $f_p = 0.28$. The particle is modeled as a 2-phase system, with fibrillation in the PB domains.

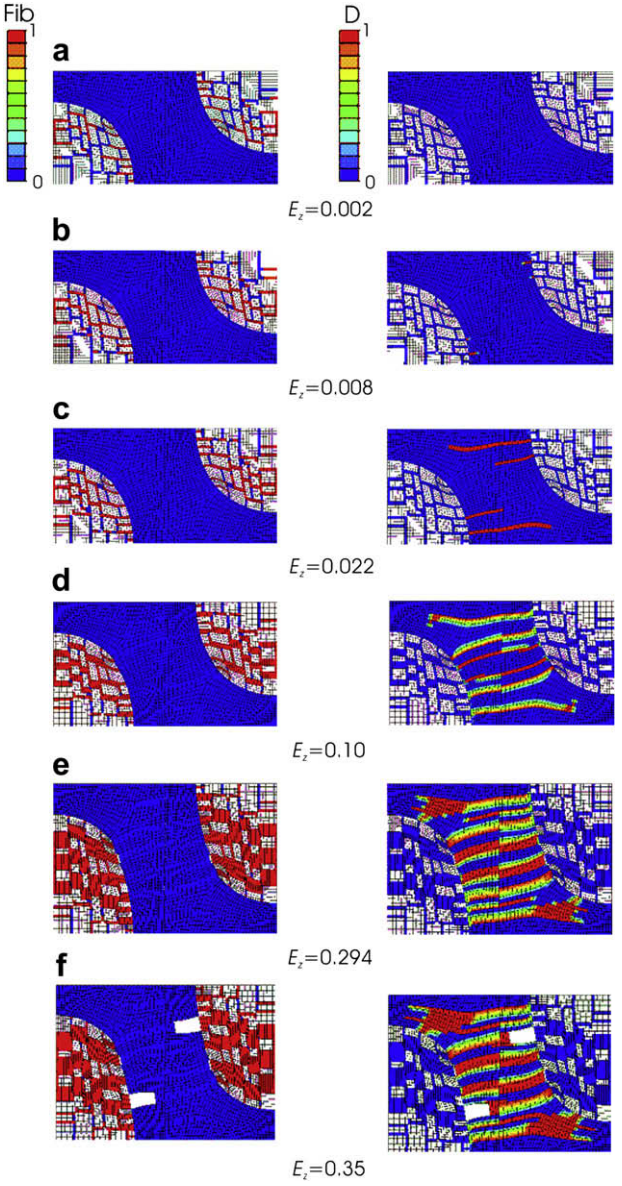

Fig. 11. Contour plots of fibrillation in PB (left), and craze profile (right) corresponding to Fig. 10.

clarifies the role of fibrillation in the deformation and toughening of HIPS. First, comparing Fig. 8 with Fig. 10, we note that in the absence of fibrillation the macroscopic stress required to initiate crazes, as well as the macroscopic yield, is higher compared to the case where the particle fibrillates. The former exhibits softening beyond the peak stress, while the latter shows a slightly hardening behavior. Typical experimental stress–strain curves for HIPS (Fig. 1(a)) are consistent with predictions of the RVE model with particle fibrillation. Second, the absence of fibrillation renders $E_{v(particle)} \cong 0$, which is not in line with the SAXS experiments [4,5]. When the particle is allowed to fibrillate, a substantial amount of inelastic volumetric strain is accommodated by the particle. Physically, the fibrillating particle is more compliant than the non-fibrillating particle, allowing an easy accommodation of axial stretch in the particle; this eliminates the unrealistic, pervasive crazing seen for the non-fibrillating particle models. The consequent reduced rate of craze opening in the PS matrix results in delayed craze breakdown (compared to the non-fibrillating case) and hence a tougher composite. A comparison of craze contour plots for the non-fibrillating vs. the fibrillating case indicates a more realistic (see, e.g., Fig. 1) craze pattern for the latter.

3.4. Effect of particle volume fraction

Fig. 12(A) shows the Σ_z–E_z behavior of RVEs with fibrillating particles, as a function of particle volume fraction f_p, at fixed particle size. The macroscopic yield and flow stress are predicted to increase with decreasing f_p. Cases with higher particle volume fraction ($f_p = 0.18$ and $f_p = 0.28$) show enhanced ductility as compared to the low volume fraction case ($f_p = 0.08$). These trends are broadly consistent with experimental results of Correa and de Sousa [40]. Fig. 12(B) shows the predicted $E_{v(particle)}$–E_z response as a function of f_p. While the overall volume change is independent of f_p, the volumetric strain contributions of matrix and particle change with f_p. In particular, with increasing f_p, $E_{v(particle)}$ increases (and $E_{v(matrix)}$ decreases), thereby lessening the accommodation of axial strain by craze opening. This results in delayed craze breakdown and delayed macroscopic failure in HIPS. The contour plots for craze damage at $E_z = 0.144$, shown in Fig. 13, indicate a more localized pattern of crazing for the case $f_p = 0.08$.

4. Summary and conclusions

The objective of this work was to investigate the role of particle morphology on the deformation and toughness of HIPS. To this end,

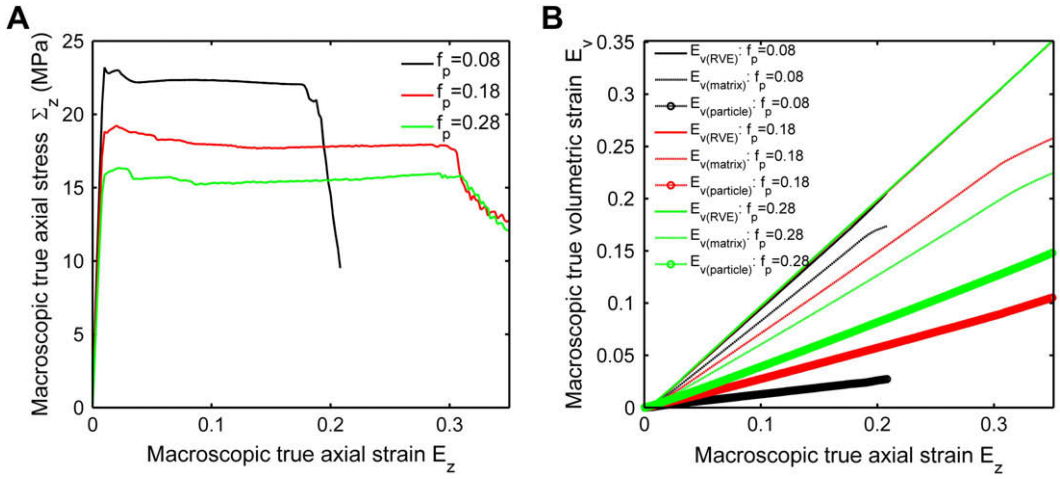

Fig. 12. (A) & (B) The predicted effect of volume fraction on the macroscopic deformation and toughness of HIPS.

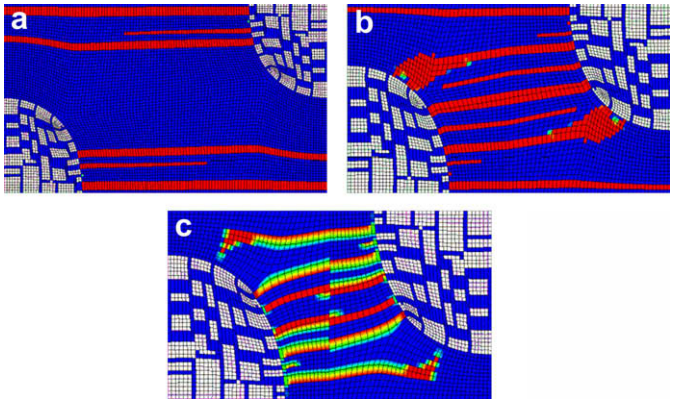

Fig. 13. Craze damage contour plots, at $E_z = 0.144$, for (a) $f_p = 0.08$, (b) $f_p = 0.18$, and (c) $f_p = 0.28$.

a one-particle axisymmetric RVE model [11] was used to independently study the effect of the following factors: (a) particle compliance, (b) particle heterogeneity, and (c) particle fibrillation.

To study the effect of particle compliance, a parametric study was conducted in which the shear modulus was systematically increased, starting from the shear modulus of neat PB. The study provided a micromechanical interpretation for the experimental finding [37] that homogeneous, compliant PB particles do not toughen PS. Next, to investigate the role of particle heterogeneity, both the PB and the PS phases of the particle were modeled, but the fibrillation of the PB domains was suppressed. The macroscopic stress–strain behavior predicted from this study showed unreasonably large yield stresses, and a softening behavior not consistent with experimental observations on HIPS. Further, the model predicted pervasive and unrealistic crazing in the PS matrix, although the craze patterns for the heterogeneous particles (for small strains) were superior, compared to the predicted craze patterns for the homogeneous/homogenized particle. An important conclusion of this study was that particle heterogeneity is an important ingredient in initiating multiple crazes from a particle, but it alone cannot adequately explain the deformation and toughness of HIPS, since it ultimately leads to unrealistic, pervasive crazing.

Finally, the PB domains in the heterogeneous "salami" particles were allowed to fibrillate. Encouragingly, the predicted Σ_z–E_z response is well in line with experiments. The substantial volume change in the particles is consistent with the SAXS experiments [4,5], as well as numerous TEM micrographs that show fibrillation in the particle. These TEM micrographs show that the initiated crazes in the PS matrix almost invariably adjoin fibrillated regions of the particle. This feature is mirrored by model predictions. Increasing particle volume fraction improves the ductility, and is associated with an increase in $E_{v(particle)}$ for a given macroscopic axial strain. The central conclusion of this work is that both particle heterogeneity and particle fibrillation are necessary to account for the deformation and toughness of HIPS.

References

[1] Dagli G, Argon AS, Cohen RE. Polymer 1995;36:2173–80.
[2] Bucknall CB. Journal of Microscopy 2001;201:221–9.
[3] Bucknall CB, Smith RR. Polymer 1965;6:437–46.
[4] Bubeck RA, Buckley DJ, Kramer EJ, Brown HR. Journal of Materials Science 1991;26:6249–59.
[5] Magalhaes AML, Borggreve RJM. Macromolecules 1995;28:5841–51.
[6] Cieslinski RC. 8th International Conference on Deformation Yield and Fracture of Polymers 1991.
[7] Bucknall CB, Soares VLP. Journal of Polymer Science, Part B: Polymer Physics 2004;42:2168–80.
[8] Socrate S, Boyce MC, Lazzeri A. Mechanics of Materials 2001;33:155–75.
[9] Zairi F, Nait-Abdelaziz M, Gloaguen JM, Lefebvre JM. 13th International Conference on Deformation, Yield and Fracture of Polymers 2006.
[10] Zairi F, Nait-Abdelaziz M, Woznica K, Gloaguen JM. European Journal of Mechanics of Solids 2005;24:169–82.
[11] Maestrini C, Callaioli A, Castellani L, Ferrando A. Journal of Materials Science 1999;34:6045–61.
[12] Rios-Guerrero L, Keskkula H, Paul DR. Polymer 2000;41:5415–21.
[13] Socrate S, Boyce MC. Journal of the Mechanics and Physics of Solids 2000; 48:233–73.
[14] Danielsson M, Parks DM, Boyce MC. Journal of the Mechanics and Physics of Solids 2002;50:351–79.
[15] Tvergaard V. Journal of the Mechanics and Physics of Solids 1996;44:1237–53.
[16] Tvergaard V. International Journal of Solids and Structures 1998;35:3989–4000.
[17] Tzika PA, Boyce MC, Parks DM. Journal of the Mechanics and Physics of Solids 2000;48:1893–929.
[18] Sharma R. Micromechanics of toughening in polymeric composites. Ph.D. thesis, Massachusetts Institute of Technology 2006.
[19] Fond C, Schirrer R. Journal of Polymer Science, Part B: Polymer Physics 2004; 42:1476–86.
[20] Boyce MC, Argon AS, Parks DM. Polymer 1987;28:1680–94.
[21] Argon AS, Cohen RE, Gebizlioglu OS. In: Yan MG, Zhang SH, Zheng ZM, editors. Mechanical behavior of materials – V, vol. 1. Oxford: Pergamon Press; 1987. p. 3.
[22] Arruda EM, Boyce MC. Journal of the Mechanics and Physics of Solids 1993; 41:389–412.
[23] Gent AN, Lindley PB. Proceedings of the Royal Society of London 1958; 249:195–205.
[24] Gent AN, Wang C. Journal of Materials Science 1991;26:3392–5.
[25] Rabinowitz S, Beardmore P. Craze formation and fracture in glassy polymers. In: Baer E, editor. Critical reviews macromolecular science, vol. 1. Cleveland, Ohio: CRC Press/Chemical Rubber Co.; 1972.

[26] Kambour RP. Advances in Polymer Science 1973;7:1–154.
[27] Kramer EJ. Advances in Polymer Science 1983;52-53:1–56.
[28] Narisawa I, Yee AF. In: Cahn RW, Haasen P, Kramer EJ, editors. Materials science and technology. A comprehensive treatment, vol. 12. New York: VCH Publishers; 1993. p. 701–64.
[29] Argon AS. In: Cahn RW, Haasen P, Kramer EJ, editors. Materials science and technology. A comprehensive treatment, vol. 12. New York: VCH Publishers; 1993. p. 461–508.
[30] Donald AM. In: Haward RN, Young RJ, editors. The physics of glassy polymers. 2nd ed. Chapman and Hall; 1997. p. 295–341.
[31] Estevez R, Tijssens MGA, Van der Giessen E. Journal of the Mechanics and Physics of Solids 2000;48:2585–617.
[32] Tijssens MGA, Van der Giessen E, Sluys LJ. Mechanics of Materials 2000;32:19–35.
[33] Tijssens MGA, Van der Giessen E, Sluys LJ. International Journal of Solids and Structures 2000;37:7307–27.
[34] Gearing BP, Anand L. International Journal of Solids and Structures 2004; 41:3125–50.
[35] Sharma R, Boyce MC, Socrate S. International Journal of Solids and Structures 2008;45:2173–202.
[36] Piorkowska E, Argon AS, Cohen RE. Macromolecules 1990;23:3838–48.
[37] Donald AM, Kramer EJ. Journal of Applied Polymer Science 1982;27:3729–41.
[38] Bucknall CB. Toughened plastics. London: Applied Science Publishers Ltd; 1977.
[39] G'Sell CG, Hiver JM, Dahoun A. International Journal of Solids and Structures 2002;39:3857–72.
[40] Correa CA, de Sousa JA. Journal of Materials Science 1997;32:6539–47.